ACS Energy LETTERS

Cite This: ACS Energy Lett. 2018, 3, 1307−1314

LETTER

Hybrid Tandem Quantum Dot/Organic Solar Cells with Enhanced Photocurrent and Efficiency via Ink and Interlayer Engineering

Taesoo Kim,[†] Yuliar Firdaus,[†] Ahmad R. Kirmani,[†] Ru-Ze Liang,[†] Hanlin Hu,[†] Mengxia Liu,[‡] Abdulrahman El Labban,[†] Sjoerd Hoogland,[‡] Pierre M. Beaujuge,[†] Edward H. Sargent,[‡] and Aram Amassian*[,†]

[†]KAUST Solar Center (KSC), and Physical Sciences and Engineering Division, King Abdullah University of Science and Technology (KAUST), Thuwal 23955-6900, Saudi Arabia

[‡]Department of Electrical and Computer Engineering, University of Toronto, Toronto, Ontario M5S 3G4, Canada

Supporting Information

ABSTRACT: Realization of colloidal quantum dot (CQD)/organic photovoltaic (OPV) tandem solar cells that integrate the strong infrared absorption of CQDs with large photovoltages of OPVs is an attractive option toward high-performing, low-cost thin-film solar cells. To date, monolithic hybrid tandem integration of CQD/OPV solar cells has been restricted due to the CQD ink's catastrophic damage to the organic subcell, thus forcing the low-band-gap CQD to be used as a front cell. This suboptimal configuration limits the maximum achievable photocurrent in CQD/OPV hybrid tandem solar cells. In this work, we demonstrate hybrid tandem solar cells employing a low-band-gap CQD back cell on top of an organic front cell thanks to a modified CQD ink formulation and a robust interconnection layer (ICL), which together overcome the long-standing integration challenges for CQD and organic subcells. The resulting tandem architecture surpasses previously reported current densities by ∼20−25% and yields a state-of-the-art power conversion efficiency (PCE) of 9.4%.

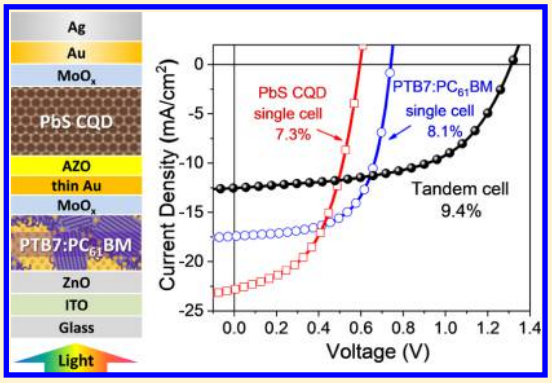

Organic and colloidal quantum dot (CQD) light absorbers are attractive solution-processed materials for thin-film photovoltaics (PV), enabling roll-to-roll manufacturing of cost-effective lightweight modules at low temperature.[1−8] Individual materials are currently limited to ca. 13% certified power conversion efficiency (PCE) in single-junction solar cells.[9−12] Multijunction solar cell architectures can harvest a larger portion of the solar spectrum.[13−19] CQD solids benefit from a size-tunable band gap that allows absorption of a wide range of wavelengths from visible to near-infrared.[4−8,11] Meanwhile, organic absorbers tend to have a narrower spectral absorption compared to quantum dot solids,[1,2,9,10,20] making them especially attractive for multi-junction CQDs and organic solar cells, especially if materials are selected to exhibit complementary light absorption properties. In recent years, CQD/organic hybrid tandem solar cells have been monolithically integrated and reported by several groups.[21−26] However, one noteworthy limitation in all of the reports has been the unusual placement of the low-band-gap CQD subcell as the front cell, namely, on the transparent electrode-coated glass substrate, limiting the ability of the tandem to generate higher photocurrent. The primary reason constraining researchers to this architecture is the incompatibility of the CQD ink solvents with underlayers, including the bulk heterojunction (BHJ) organic photoactive layer and the interconnection layers (ICLs).[22−25] The secondary, yet still important, reason is the need for repeated solid-state ligand exchange in many legacy recipes for the CQD active layer or for the CQD hole transporting layer (HTL).[4,5,8,11] Ligand exchange, which significantly densifies the CQD film, has been shown to cause additional chemical damage and stress-induced cracking of underlayers.[22−24] Tong et al. have suggested top-illumination in CQD/organic hybrid tandem solar cells using transparent indium-doped tin oxide (ITO) bottom and PEDOT:PSS top electrodes, respectively.[24] However, illuminating from the top still resulted in poorly performing devices because the illumination direction strongly affects the light harvesting by the depleted heterojunction

Received: March 22, 2018
Accepted: May 3, 2018
Published: May 3, 2018

DOI: 10.1021/acsenergylett.8b00460
ACS Energy Lett. 2018, 3, 1307−1314

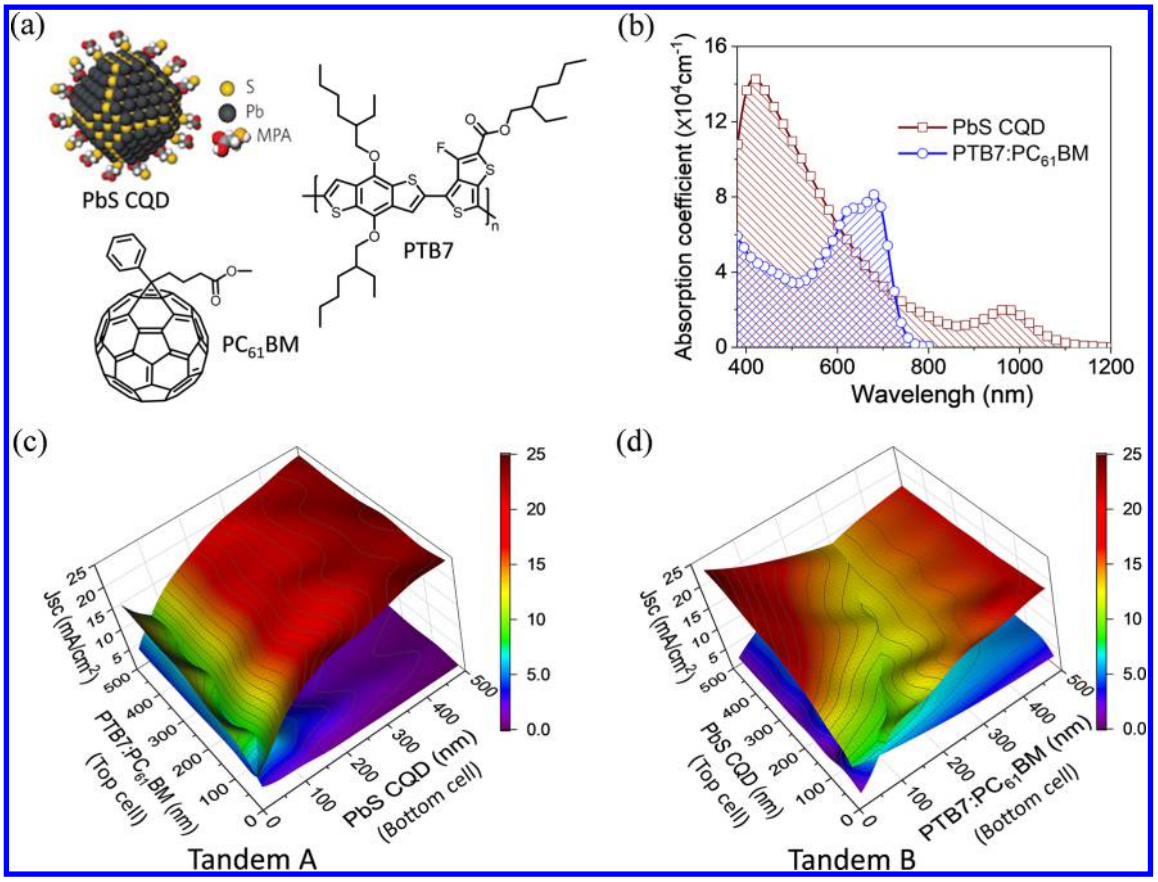

Figure 1. (a) Materials chart: PbS quantum dots after ligand exchange, the polymer donor PTB7, and the fullerene acceptor $PC_{61}BM$. (b) Absorption coefficients of the PbS CQD and the PTB7:$PC_{61}BM$ active layers. Simulated J_{SC} of the hybrid tandem solar cells depending on the device structures: (c) PbS CQD active layer as the front cell and organic active layer as the back cell (Tandem A); (d) PbS CQD active layer as the back cell and organic active layer as the front cell (Tandem B). The cross-matched intersection of the surface plot shows the current-matched values achievable in each case, giving a 30% advantage to Tandem B. The contour is drawn with 1 mA/cm^2 increments.

(DHJ) CQD subcell.[27,28] This favors illumination through the n-type electron transporting layer (ETL), which is typically at the bottom of n−p and n−i−p CQD solar cells, placing additional constraints on the subcell and hybrid tandem configurations. We have taken the view that overcoming these challenges and successfully integrating solution-processed low-band-gap CQD solar cells on top of the organic front cell is crucial to realize highly efficient tandem solar cells that surpass the performances of state-of-the-art single-junction CQDs or organic solar cells. Indeed, two-terminal hybrid tandem solar cells are predicted to achieve a 30% higher photocurrent for the same active materials simply by switching the CQD subcell to the back and placing the organic photovoltaic (OPV) subcell at the front (Figure 1).

In this Letter, we successfully overcome the challenges of monolithic integration of a low-band-gap CQD subcell directly on top of a high-band-gap organic front cell to achieve state-of-the-art PCE for hybrid tandem CQD/OPV solar cells by experimentally achieving a 20−25% increase of the photocurrent as compared to the previously reported values to date.[21−23,25,26] To do so, we designed a modified CQD ink formulation and a robust electrical ICL, which are compatible and preserve the integrity of the underlying OPV front cell. The reformulated CQD ink utilizes hexane,[25] which reduces damage to the delicate organic BHJ layer and cuts the number of steps required for CQD layer deposition, better preserving the integrity of all underlayers, including the ICL. The tandem's open-circuit voltage (V_{OC}) of 1.31 V is equal to the sum of subcell voltages, while the photocurrent of 12.5 mA/cm^2 and the PCE of 9.4% are the highest reported to date in CQD/organic hybrid tandem solar cells.[21−26] The tandem PCE significantly surpasses those of the organic (8.1%) and CQD (7.3%) subcells, highlighting the success of the integration approach. This successful demonstration is an important milestone for the monolithic integration of state-of-the-art CQD and organic solar cells into tandem devices that can one day outperform the best single-junction solar cells in each field.

In Figure 1a, we show the material systems used in this study: the chemical structures of the polymer donor, thieno-[3,4-*b*]thiophene/benzodithiophene (PTB7), and fullerene acceptor, [6,6]-phenyl-C_{60}-butyric acid methyl ester ($PC_{61}BM$),[29−31] as well as a PbS CQD with an organic 3-mercaptopropionic acid (MPA) ligand.[32,33] The high-resolution transmission electron microscopy (TEM) image of PbS CQDs before ligand exchange is shown in Figure S1 (average CQD size: ∼3.5 nm). PTB7 was used in conjunction with $PC_{61}BM$ to form the polymer:fullerene organic BHJ subcell. The absorption coefficients of the PTB7:$PC_{61}BM$ and PbS CQD active layers are shown in Figure 1b. The CQD layer shows relatively strong absorption in the short-wavelength visible range and weaker absorption in the red and NIR with an exciton peak at 970 nm, while the PTB7:$PC_{61}BM$ subcell transmits, to some extent, the visible spectrum at around 500 nm and then absorbs effectively in the red regions (up to 750

DOI: 10.1021/acsenergylett.8b00460
ACS Energy Lett. 2018, 3, 1307−1314

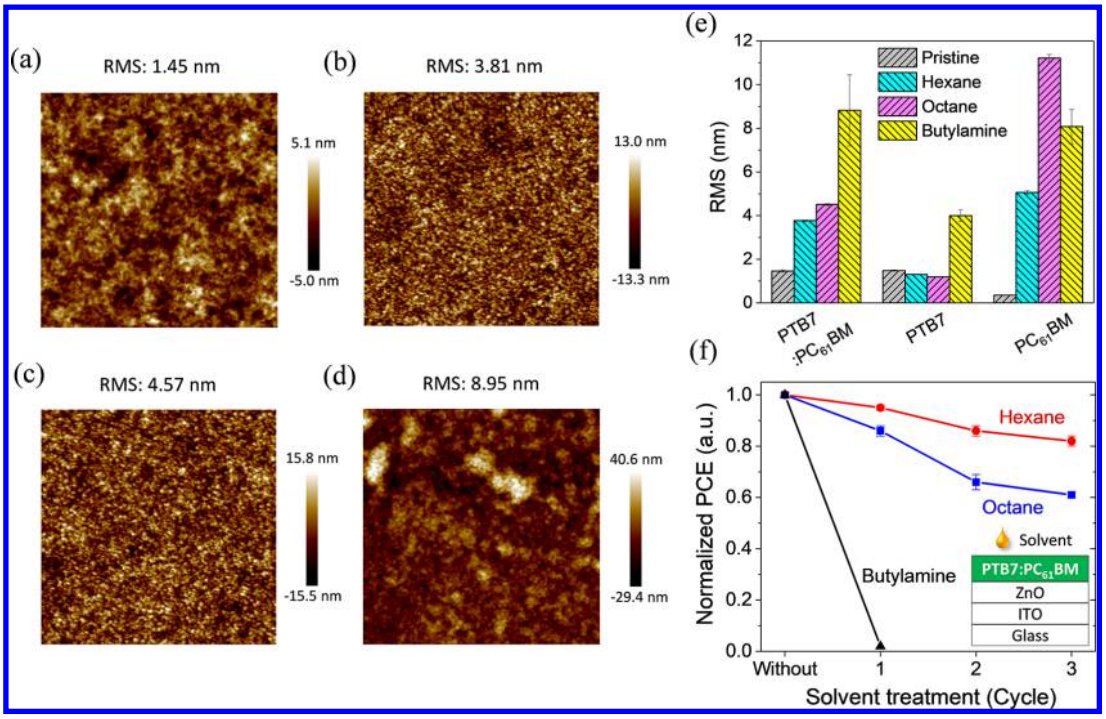

Figure 2. AFM images of the PTB7:$PC_{61}BM$ surface topography, (a) before solvent treatment and after treatment with (b) hexane, (c) octane, and (d) butylamine. The scan size is 5 μm × 5 μm. (e) Summary of the RMS surface roughness of solvent-treated organic thin films of PTB7:$PC_{61}BM$, only PTB7, and only $PC_{61}BM$. (f) Normalized PCE of organic single-junction cells without and with direct solvent treatment of the photoactive layers (without a protective ICL).

nm), compensating for the CQD layer's weaker absorption in the red regions. The spectral responses of the two active layers are thus reasonably complementary.[25]

In previous reports on CQD/organic hybrid tandem solar cells, the device architectures have been configured such that the CQD subcell is located at the bottom, i.e., on the transparent substrate, while the organic subcell is fabricated above.[21−26] This forces the incident light to be absorbed first by the low-band-gap CQD layer with the remaining light transmitted through the ICL and absorbed by the organic active layer.[21−23,25,26] Importantly, the J_{SC} of the tandem device is limited in this configuration, despite the partial spectral complementarity of the active layers, limiting, in turn, the achievable PCE by the tandem device as compared to the individual CQD and organic single-junction cells. Optical simulations were performed to compare the two CQD/organic hybrid tandem architectures, with tandem A (Figure S2a) placing the CQD subcell at the bottom side as front cell[22,23,25,26] and tandem B (Figure S2b) placing it at the top side as back cell. The device structures, layer thicknesses, and optical constants are depicted in Figure S2. The simulated current densities of tandems A and B are shown in Figures 1c,d, respectively, for active layer thicknesses ranging from 0 to 500 nm, with light incidence from the glass substrate side in both scenarios. The simulations predict a J_{SC} as high as ca. 10 mA/cm^2 for tandem A and ca. 13 mA/cm^2 for tandem B and identify optimal subcell thicknesses for these scenarios, clearly showing a 30% advantage for tandem B. Hence, the complementary absorption by the two active layers is more effective in tandem B than in tandem A. The ca. 30% advantage of tandem B in terms of J_{SC} motivates its fabrication but poses serious challenges from the monolithic integration perspective. In particular, the bottom organic active layer is easily dissolved or damaged by some of the solvents typically used for CQD coating and/or ligand exchange, imposing important restrictions on the CQD ink and its coating process.[21−26] We have set out to investigate alternative CQD ink solvents and robust ICLs that can survive the CQD coating process and provide protection for all underlayers.

Octane and butlyamine are the two most commonly used solvents for conventional PbS CQD solar cells.[4−8,11,25,32,33] In Figure 2, we investigate and compare the effects of exposure to two common CQD solvents (octane and butylamine) on the morphology of the organic BHJ layer and the operational stability of a single-junction organic solar cell. For this purpose, we exposed the PTB7:$PC_{61}BM$ BHJ layers directly to blank solvents, which were cast and spun off the organic photoactive layers in a manner that simulates CQD coating conditions. The solvent treatments were performed in the absence of the ICL in order to simulate the worst case scenario of solvent damage. We assessed the solvent effects on BHJ morphology by performing atomic force microscopy (AFM) measurements of the surface topography before and after exposure to each solvent. We subsequently fabricated single-junction organic solar cells using similarly solvent-treated photoactive layers (see the experimental section in the Supporting Information for the solvent treatment method). In Figure 2a, we see AFM images of the surface morphology of an as-prepared PTB7:$PC_{61}BM$ active layer, exhibiting a root-mean-squared (RMS) roughness of 1.45 nm. Micrographs in Figure 2b−d show that the BHJ layer roughens moderately in the case of octane and very significantly in the case of butylamine, indicative of significant solvent−BHJ interactions. We summarize in Figure 2e, the RMS surface roughness of pristine PTB7, $PC_{61}BM$, and PTB7:$PC_{61}BM$ blend layers and after solvent treatment. AFM images of PTB7 and $PC_{61}BM$ before and after solvent treatment are presented in Figure S3. The data attribute the increasing RMS roughness of the PTB7:$PC_{61}BM$ blend to

DOI: 10.1021/acsenergylett.8b00460
ACS Energy Lett. 2018, 3, 1307−1314

partial solubility of $PC_{61}BM$ in octane, whereas butylamine dissolves both the PTB7 and $PC_{61}BM$.

These changes to the active layer's morphology understandably impact the operation of organic solar cells. We plot the normalized PCE of the solvent-treated PTB7:$PC_{61}BM$ single-junction cells with respect to the number of solvent treatments in Figure 2f. A one-time exposure to butylamine is sufficient to render the solar cell inoperable, whereas octane exposure is less invasive but reduces efficiency by 40% after three treatments. Even when butylamine solvent treatment was applied indirectly through the ICL (see below for detailed selection criteria of ICL) in a simulated solar cell stack (glass/ITO/PTB7:$PC_{61}BM$/MoO_x/thin Au/AZO) (Figure S4b,c), it caused significant damage by dissolving the organic layer. Octane had a far less dramatic but non-negligible effect. Fortunately, MPA in acetonitrile (ACN) treatment used to simulate the CQD ligand exchange did not show a negative effect on organic device performance (Figure S4a).[33] We therefore conclude that the latest, most modern CQD inks based on butylamine are particularly difficult to apply at this stage in the tandem B architecture, with octane emerging as a better choice, but one that is still unacceptable because it reduces the operational performance of the OPV subcell through the protective ICL.

Addressing these issues requires a solvent that can disperse CQDs and minimize harmful interactions with the underlying OPV subcell and the ICL. We propose hexane as an alternative solvent because it is considered a marginal solvent for many organic semiconductors. Hexane also has the advantage of a much lower boiling point (68 °C) than octane (125 °C), allowing it to dry much faster and minimize solvent liquid−OPV interactions during CQD spin-coating. Indeed, we show in Figure 2 that hexane appears to induce the smallest morphological changes to the organic photoactive layer among all three solvents. Hexane is also found to have minimal effect on the ICL compared to octane and butylamine (Figure S4b−d). Importantly, hexane exposure shows the smallest loss on OPV devices, with a 5% drop in PCE after a single direct treatment and 20% drop in PCE after three cycles of solvent treatment. These losses should be mitigated further by the protective ICL.

The fast-drying solvent has an additional mitigating benefit by reducing the number of CQD coating steps. CQD films coated using octane- and hexane-based inks of identical concentration (50 mg/mL) result in a final CQD thickness (after MPA ligand exchange) of 40 nm (2500 rpm) when using octane[22] and 100 nm (3000 rpm) when using hexane. This difference is ascribed to the rapid drying and solidification of the ink, which reduces the time window within which the ink can be ejected during the spin-up and outflow regimes of spin-coating.[34] The ability of hexane to decrease the number of CQD coating cycles required to achieve thicker films needed for the tandem B architecture can thus significantly reduce the potential damage to underlayers compared to octane by a combination of reduced interaction strength and interaction time. The choice of hexane forces the use of a legacy CQD DHJ top cell using a hexane-based ink and MPA ligand exchange as the most suitable approach for successful monolithic integration of a CQD back cell on top of the OPV front cell.

The design and selection of the ICL to connect the CQD back cell to the underlying organic front cell was also significantly constrained by the same stringent requirements posed by the CQD deposition and ligand exchange on top of the ICL and organic underlayers. These constraints are as follows: (1) sensitivity to solvents used in the CQD layer deposition,[22,24] (2) sensitivity to heat as PTB7 (and many related donor materials) does not fare well under thermal annealing or high-temperature deposition,[35] and (3) sensitivity to mechanical stresses induced by solid-state ligand exchange.[36] The low-temperature processing requirement excludes the use of popular interlayers, such as sol−gel ZnO and TiO_2 as the ETL and PEDOT:PSS as the HTL, due to their thermal annealing requirements.[13,37−40] The mechanical stress resistance requirement also excludes most organic interlayers and films processed by thermal evaporation at the expense of sputtering at low temperature. However, organic semiconductors are easily damaged by sputtering, requiring the first layer of the ICL in direct contact with the organic BHJ layer to be vacuum-evaporated instead and be sufficiently robust to withstand subsequent sputtering.[41] For these reasons, we have opted for a trilayer ICL with vacuum-evaporated MoO_x on the organic side and a metal oxide ETL on the CQD side.[18,19,23,41−44] The central layer of the ICL was an ultrathin (0.5 nm) Au layer that breaks up into islands acting as effective recombination sites,[42−44] as will be discussed below. We have opted for Al-doped ZnO (AZO) deposited by RF-sputtering as the n-type ETL.[25] The conductivity of the AZO layer used here was $\leq 10^{-7}$ S/cm. Figure S5 shows the significant damage to alternative metal oxide nanoparticle (NP) layers based on solution-processed AZO and ZnO NPs instead of sputtered AZO. Therefore, the compact and dense AZO produced by sputtering was preferred over solution-processed nanocrystal metal oxides such as AZO, TiO_2, ZnO, etc. as these often yield less compact films that can be easily permeated or delaminated by the CQD ink and/or be harmed by the mechanical stress buildup in the CQD overlayer after ligand exchange. The oleic acid-capped PbS CQD active layer deposited from the hexane-based formulation was ligand-exchanged using MPA in ACN and was repeated until the desired thickness was reached. The tandem stack was completed by vacuum evaporation of MoO_x as the HTL and Au/Ag as the anode.[25,33]

In Figure 3a, we present the hybrid tandem B device schematic and show a cross-sectional TEM image of the actual device based on a 200 nm thick PTB7:$PC_{61}BM$ bottom active layer and a 300 nm PbS CQD (3 layers) active layer. The device includes a ZnO/ITO cathode, a MoO_x/Au/Ag anode, and the trilayer MoO_x/thin Au/AZO ICL. The energy level diagram of the hybrid tandem device is presented in Figure 3b. The PTB7:$PC_{61}BM$ active layer was spun-cast on top of a sol−gel ZnO layer also prepared by spin-coating on ITO-coated glass. The ICL consists of a stack of MoO_x/thin Au/AZO. MoO_x was vacuum-deposited on PTB7:$PC_{61}BM$ to form the HTL. An ultrathin Au layer (0.5 nm) was deposited by thermal evaporation with careful thickness monitoring. As shown in Figure 3b, the Au layer forms an asymmetric work function within the ICL, which grades the work function from high on the MoO_x side (to promote hole injection from the organic photoactive layer into the ICL) to low work function on the AZO side (to promote electron injection from the CQD photoactive layer into the ICL).[18,19,23] The ultrathin Au layer forms nanoislands, as seen in SEM and AFM measurements (Figure S6). These act as efficient recombination sites and reduce the accumulation of photoexcited charges in the photoactive layers and near the ICL.[18,19,23,41−44] The fill factor (FF) and thus the performance of tandem cells benefits strongly from the presence of Au nanoislands,[18,19,23,25] as

DOI: 10.1021/acsenergylett.8b00460
ACS Energy Lett. 2018, 3, 1307−1314

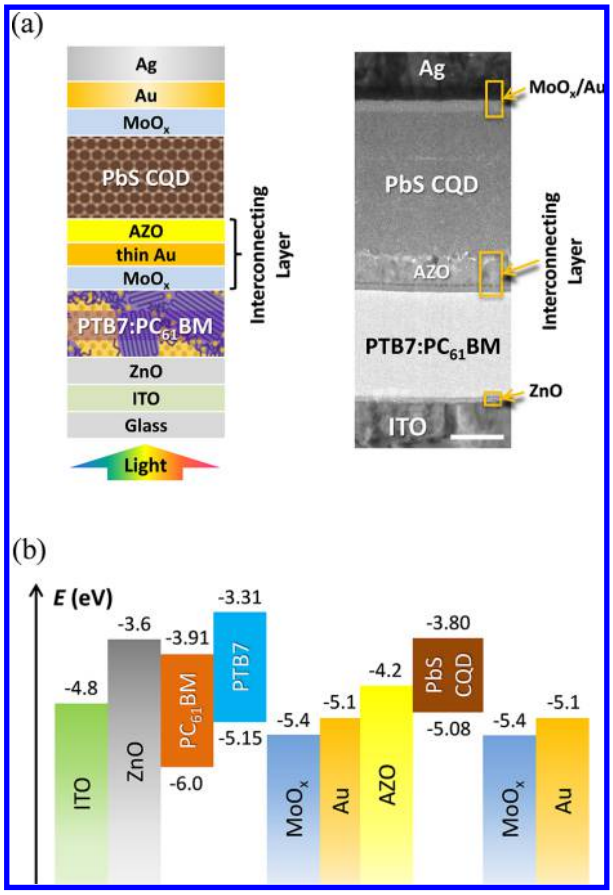

Figure 3. (a) Hybrid tandem solar cell configuration and TEM cross-sectional image of the corresponding device. The scale bar is 100 nm. (b) Energy level diagram of the hybrid tandem solar cell.

shown in Figure S7a of tandem solar cells prepared without and with Au nanoislands within the ICL. Figure S7b compares the conductance of ICL including a thin Au layer as compared to an ICL without Au and shows that the inclusion of Au reduces the series resistance of the ICL.[18,19,23,25] The device structures used for these conductance measurements were the isolated interlayer stacks, including glass/ITO/MoO_x/Au (0.5 nm)/AZO/Al and glass/ITO/MoO_x/AZO/Al.

Individual single-junction cells were first fabricated employing organic or CQD photoactive layers with different thickness using the same ETL and HTL as those in the tandem B architecture. The configurations for the PbS CQD and organic single cells were glass/ITO/AZO/PbS CQD/MoO_x/Au/Ag and glass/ITO/ZnO/PTB7:PC_{61}BM/MoO_x/Ag, respectively. In Figure 4a, we show current density−voltage (J−V) curves obtained for CQD and organic single-junction cells depending on active layer thicknesses ranging from 100 to 500 nm for the former and 145 to 210 nm for the latter. The summary of statistical device parameters of the organic and CQD single-junction cells is presented in Figures S8 and S9, respectively, while all parameters are summarized in Table 1. The organic active layer thickness was varied by changing the spin-coating speed, whereas the CQD active layer thickness was varied by repeating the CQD coating and ligand exchange processes, which incremented the thickness by 100 nm per cycle. In organic cells, increasing the active layer thickness leads to higher J_{SC} at the expense of the FF, with the PCE showing a small drop due to the trade-off between J_{SC} and the FF within the thickness range studied (Table 1). The single-junction CQD cells also show a similar trend, with higher J_{SC} in thicker active layers with the FF and PCE showing maximum values for a 300 nm thickness (Table 1). Looking into the V_{OC} of PbS CQD single-junction cells, such materials are known for exhibiting significant energetic losses that lead to poor output voltages corresponding to the band gap. Fundamentally, the voltage loss mechanism in CQDs is directly related to the large number of surface atoms (due to the high surface-to-volume ratio), which result in a high density of band tails. The solid-state ligand exchange further enhances these band tails due to an increased morphological disorder. Guyot-Sionnest has theoretically suggested that the extent of band tails currently found in legacy CQD solids (obtained by solid-state ligand exchange) limits the maximum achievable output voltage to 50% of the CQD band gap.[45] Therefore, a ∼0.58 V output voltage for our CQD cells employing PbS CQDs with a ca. 1.2 eV band gap is close to the theoretical optimum.

On the basis of the experimental results for single-junction organic and CQD cells with re-engineered CQD ink, we have monolithically integrated CQD/organic subcells into the tandem B architecture shown in Figure 3a, namely, glass/ITO/ZnO/PTB7:PC_{61}BM/MoO_x/ultrathin Au/AZO/PbS CQD/MoO_x/Au/Ag. The thicknesses of both CQD and organic active layers were varied to maximize current matching and achieve the highest PCE. Fixing the organic active layer thickness to 190 nm, the FF decreased and the J_{SC} saturated with increasing CQD active layer thickness up to 500 nm (Figure S10, Table 1). By contrast, fixing the CQD layer thickness to 300 nm and increasing the organic active layer thickness up to 210 nm, the FF decreased while J_{SC} peaked at a thickness of 200 nm (Figure 4b,c, Table 1). Importantly, the V_{OC} was nearly constant without significant photovoltage drops, independent of either of the active layer thicknesses. This is significant as it indicates that the ICL and the organic subcell can survive up to five repeated CQD coating and ligand exchange steps without serious damage to the device.

The optimized hybrid tandem solar cell yielded a V_{OC} of 1.31 V, a FF of 56.7%, and a J_{SC} of 12.5 mA/cm^2 with high current matching, leading to a PCE of 9.3% on average and a best PCE value of 9.4%. This is achieved with a 200 nm thick organic active layer and a 300 nm thick CQD active layer. The photocurrent is the highest achieved to date and surpasses by ∼20−25% the previous reported photocurrent values,[21−23,25,26] in reasonably good agreement with optical simulations reported in Figure 1. The shunt and series resistances of the optimized tandem and their single cells are summarized in Table S1.

In Figure 5a, we show the J−V characteristics of single-junction and tandem cells with the same active layer thicknesses. Figure 5b shows the external quantum efficiency (EQE) for the single-junction CQD and organic cells with the thickness employed in the optimized tandem cell. The CQD cell harvests the solar spectrum in the short-wavelength region (UV/blue regions), but the EQE drops significantly from its peak at 440 nm and up to 880 nm, showing a second increase at around 970 nm, corresponding to the CQD exciton peak position before the band edge near 1200 nm. The EQE of the PTB7:PC_{61}BM cell is particularly pronounced from the green to red region for 500 < λ < 750 nm, showing complementary EQE spectra with the CQD cell. The optimized tandem solar cells exhibit significantly higher PCE than the best-performing single-junction organic (8.3%) and CQD (7.1%) cells. The tandem open-circuit voltage (V_{OC}) of 1.31 V is equal to the

DOI: 10.1021/acsenergylett.8b00460
ACS Energy Lett. 2018, 3, 1307−1314

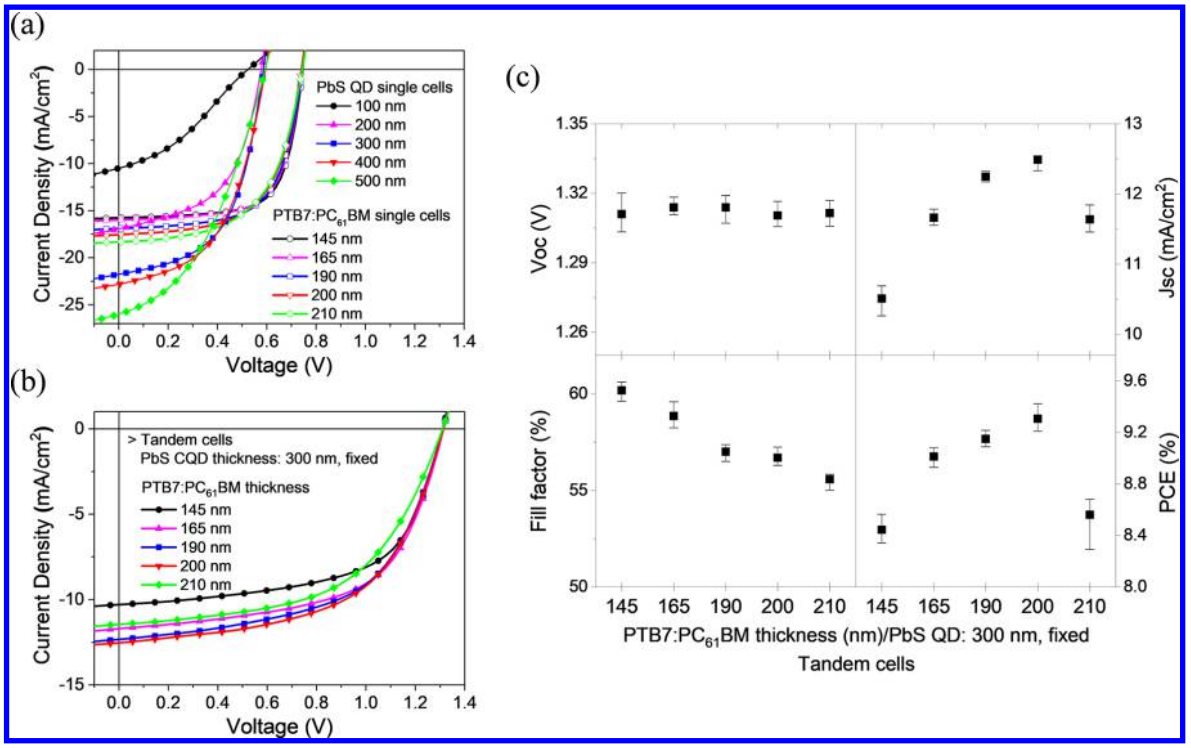

Figure 4. (a) Representative $J-V$ curves of PTB7:$PC_{61}BM$ and PbS CQD single-junction cells depending on their active layer thicknesses. (b) $J-V$ characteristics of hybrid tandem solar cells of various PTB7:$PC_{61}BM$ layer thicknesses, fixing the PbS CQD layer at 300 nm, and (c) statistical parameter summary of these tandem solar cells.

Table 1. Averaged Device Parameters of PTB7:$PC_{61}BM$, PbS CQD Single-Junction Cells, and Hybrid Tandem Solar Cells Depending on Active Layer Thicknesses[a]

device structure	active layer	thickness	V_{OC} (V)	J_{SC} (mA/cm^2)	FF (%)	PCE (%)	best PCE (%)
single cell	PTB7:$PC_{61}BM$	145 nm	0.75	15.8	69.4	8.2	8.3
		165 nm	0.75	15.9	68.1	8.1	8.2
		190 nm	0.75	16.9	64.0	8.1	8.2
		200 nm	0.74	17.4	60.8	7.9	8.1
		210 nm	0.74	18.3	58.0	7.9	8.1
	PbS CQD	100 nm	0.51	10.6	34.9	1.9	2.1
		200 nm	0.58	16.9	54.0	5.3	5.9
		300 nm	0.58	21.8	54.7	7.0	7.3
		400 nm	0.60	22.6	50.2	6.5	7.0
		500 nm	0.59	25.9	44.0	6.4	6.9
tandem cell	PTB7:$PC_{61}BM$/PbS CQD	145 nm/300 nm	1.31	10.5	60.2	8.4	8.6
		165 nm/300 nm	1.31	11.7	58.9	9.0	9.1
		190 nm/200 nm	1.31	11.1	58.6	8.6	8.7
		190 nm/300 nm	1.31	12.3	57.0	9.2	9.2
		190 nm/400 nm	1.30	12.6	54.7	8.9	9.0
		190 nm/500 nm	1.30	12.6	53.7	8.8	8.9
		200 nm/300 nm	1.31	12.5	56.7	9.3	9.4
		210 nm/300 nm	1.31	11.6	55.6	8.6	8.7

[a]Average values based on 20 devices.

sum of two single-junction cell voltages. The FF (56.7%) of the optimized tandem was found to be at an intermediate level compared with the single-junction organic (60.8%) and CQD (54.7%) cells with the same active layer thickness. These results prove that the organic and CQD subcells are effectively connected and current-matched.

In conclusion, we demonstrated the implementation of a tandem solar cell with a solution-processed PbS CQD back cell monolithically integrated through connection in series with an underlying PTB7:$PC_{61}BM$ front cell. This tandem solar cell with the CQD back cell and an OPV front cell achieves higher current matching and PCE compared to previous reports. The primary enabling breakthrough was the development of a CQD ink formulation that minimizes chemical and structural damage to the underling OPV subcell and ICL. The secondary enabling development was the design of a robust trilayer ICL that survives the chemical and mechanical stresses induced by CQD coating and ligand exchange steps while itself not damaging the delicate organic subcell. To date, this is the most efficient CQD/organic hybrid tandem structure and far exceeds the

DOI: 10.1021/acsenergylett.8b00460
ACS Energy Lett. 2018, 3, 1307−1314

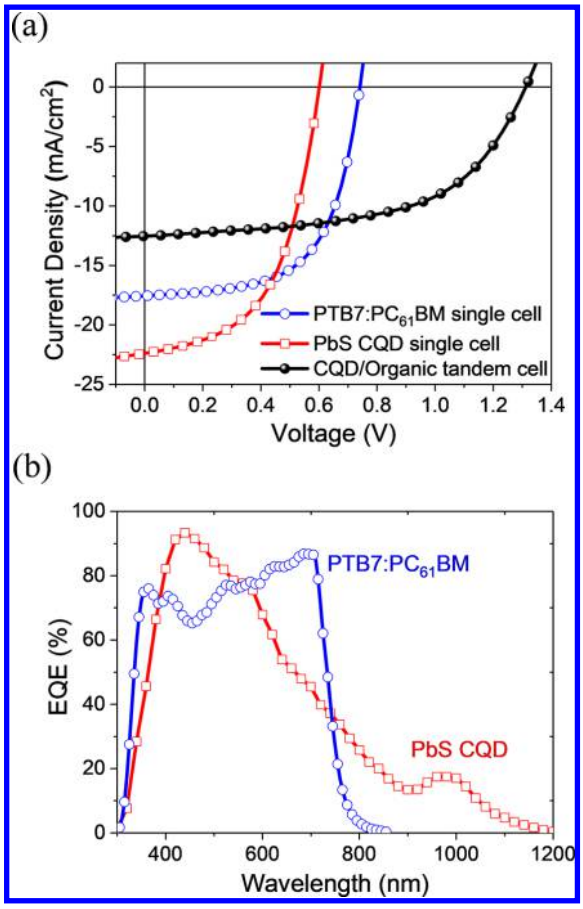

Figure 5. (a) *J*–*V* curves of optimized hybrid tandem and the single-junction cells with the same active layer thicknesses and (b) EQE spectra of the PTB7:$PC_{61}BM$ and PbS CQD single-junction cells, which were applied for the optimized tandem cells.

PCEs of individual subcells. This work is expected to pave the way for further successful integration of hybrid tandem OPV/CQD solar cells with PCE that can one day surpass the state-of-the-art PCE of each individual field.

■ ASSOCIATED CONTENT

Supporting Information

The Supporting Information is available free of charge on the ACS Publications website at DOI: 10.1021/acsenergylett.8b00460.

Experimental methods of device fabrication, electrical characterization, and AFM, TEM, and SEM images (PDF)

■ AUTHOR INFORMATION

Corresponding Author

*E-mail: aram.amassian@kaust.edu.sa. Phone: +966 12 808 4470.

ORCID

Mengxia Liu: 0000-0002-1676-705X
Pierre M. Beaujuge: 0000-0003-2868-4494
Edward H. Sargent: 0000-0003-0396-6495
Aram Amassian: 0000-0002-5734-1194

Notes

The authors declare no competing financial interest.

■ ACKNOWLEDGMENTS

This work was supported by the King Abdullah University of Science and Technology (KAUST) and the Ontario Research Fund - Research Excellence program. M.L. acknowledges support from the Hatch Research Scholarship. The authors thanks E. Palmiano at the University of Toronto for support in the synthesis of quantum dots and Dr. Seyoung Kee at KAUST for the conductivity measurement of the sputtered AZO layer.

■ REFERENCES

(1) Heeger, A. J. 25th Anniversary Article: Bulk Heterojunction Solar Cells: Understanding the Mechanism of Operation. *Adv. Mater.* **2014**, *26*, 10–28.
(2) Beaujuge, P. M.; Fréchet, J. M. Molecular Design and Ordering Effects in π-Functional Materials for Transistor and Solar Cell Applications. *J. Am. Chem. Soc.* **2011**, *133*, 20009–20029.
(3) Finn, M., III; Martens, C. J.; Zaretski, A. V.; Roth, B.; Søndergaard, R. R.; Krebs, F. C.; Lipomi, D. J. Mechanical Stability of Roll-to-Roll Printed Solar Cells under Cyclic Bending and Torsion. *Sol. Energy Mater. Sol. Cells* **2018**, *174*, 7–15.
(4) Kim, J. Y.; Voznyy, O.; Zhitomirsky, D.; Sargent, E. H. 25th Anniversary Article: Colloidal Quantum Dot Materials and Devices: A Quarter-Century of Advances. *Adv. Mater.* **2013**, *25*, 4986–5010.
(5) Wang, R.; Shang, Y.; Kanjanaboos, P.; Zhou, W.; Ning, Z.; Sargent, E. H. Colloidal Quantum Dot Ligand Engineering for High Performance Solar Cells. *Energy Environ. Sci.* **2016**, *9*, 1130–1143.
(6) MacDonald, B. I.; Martucci, A.; Rubanov, S.; Watkins, S. E.; Mulvaney, P.; Jasieniak, J. J. Layer-by-Layer Assembly of Sintered $CdSe_xTe_{1-x}$ Nanocrystal Solar Cells. *ACS Nano* **2012**, *6*, 5995–6004.
(7) Crisp, R. W.; Panthani, M. G.; Rance, W. L.; Duenow, J. N.; Parilla, P. A.; Callahan, R.; Dabney, M. S.; Berry, J. J.; Talapin, D. V.; Luther, J. M. Nanocrystal Grain Growth and Device Architectures for High-Efficiency CdTe Ink-based Photovoltaics. *ACS Nano* **2014**, *8*, 9063–9072.
(8) Chuang, C.-H. M.; Brown, P. R.; Bulović, V.; Bawendi, M. G. Improved Performance and Stability in Quantum Dot Solar Cells through Band Alignment Engineering. *Nat. Mater.* **2014**, *13*, 796–801.
(9) Li, S.; Ye, L.; Zhao, W.; Zhang, S.; Mukherjee, S.; Ade, H.; Hou, J. Energy-Level Modulation of Small-Molecule Electron Acceptors to Achieve over 12% Efficiency in Polymer Solar Cells. *Adv. Mater.* **2016**, *28*, 9423–9429.
(10) Zhao, W.; Li, S.; Yao, H.; Zhang, S.; Zhang, Y.; Yang, B.; Hou, J. Molecular Optimization Enables over 13% Efficiency in Organic Solar Cells. *J. Am. Chem. Soc.* **2017**, *139*, 7148–7151.
(11) Liu, M.; Voznyy, O.; Sabatini, R.; Garcia de Arquer, F. P.; Munir, R.; Balawi, A. H.; Lan, X.; Fan, F.; Walters, G.; Kirmani, A. R.; et al. Hybrid Organic-Inorganic Inks Flatten The Energy Landscape in Colloidal Quantum Dot Solids. *Nat. Mater.* **2017**, *16*, 258–263.
(12) Sanehira, E. M.; Marshall, A. R.; Christians, J. A.; Harvey, S. P.; Ciesielski, P. N.; Wheeler, L. M.; Schulz, P.; Lin, L. Y.; Beard, M. C.; Luther, J. M. Enhanced Mobility $CsPbI_3$ Quantum Dot Arrays for Record-Efficiency, High-Voltage Photovoltaic Cells. *Sci. Adv.* **2017**, *3*, eaao4204.
(13) Kim, J. Y.; Lee, K.; Coates, N. E.; Moses, D.; Nguyen, T.-Q.; Dante, M.; Heeger, A. J. Efficient Tandem Polymer Solar Cells Fabricated by All-Solution Processing. *Science* **2007**, *317*, 222–225.
(14) Hadipour, A.; de Boer, B.; Blom, P. W. Organic Tandem and Multi-Junction Solar Cells. *Adv. Funct. Mater.* **2008**, *18*, 169–181.
(15) Li, G.; Chang, W.-H.; Yang, Y. Low-Bandgap Conjugated Polymers Enabling Solution-Processable Tandem Solar Cells. *Nat. Rev. Mater.* **2017**, *2*, 17043.
(16) Cui, Y.; Yao, H.; Gao, B.; Qin, Y.; Zhang, S.; Yang, B.; He, C.; Xu, B.; Hou, J. Fine Tuned Photoactive and Interconnection Layers for Achieving over 13% Efficiency in a Fullerene-free Tandem Organic Solar Cell. *J. Am. Chem. Soc.* **2017**, *139*, 7302–7309.
(17) Wang, X.; Koleilat, G. I.; Tang, J.; Liu, H.; Kramer, I. J.; Debnath, R.; Brzozowski, L.; Barkhouse, D. A. R.; Levina, L.; Hoogland, S.; et al. Tandem Colloidal Quantum Dot Solar Cells

DOI: 10.1021/acsenergylett.8b00460
ACS Energy Lett. 2018, 3, 1307–1314

Employing a Graded Recombination Layer. *Nat. Photonics* **2011**, *5*, 480−484.
(18) Choi, J. J.; Wenger, W. N.; Hoffman, R. S.; Lim, Y. F.; Luria, J.; Jasieniak, J.; Marohn, J. A.; Hanrath, T. Solution-Processed Nanocrystal Quantum Dot Tandem Solar Cells. *Adv. Mater.* **2011**, *23*, 3144−3148.
(19) Shi, G.; Wang, Y.; Liu, Z.; Han, L.; Liu, J.; Wang, Y.; Lu, K.; Chen, S.; Ling, X.; Li, Y.; et al. Stable and Highly Efficient PbS Quantum Dot Tandem Solar Cells Employing a Rationally Designed Recombination Layer. *Adv. Energy Mater.* **2017**, *7*, 1602667.
(20) Moreels, I.; Lambert, K.; Smeets, D.; De Muynck, D.; Nollet, T.; Martins, J. C.; Vanhaecke, F.; Vantomme, A.; Delerue, C.; Allan, G.; et al. Size-Dependent Optical Properties of Colloidal PbS Quantum Dots. *ACS Nano* **2009**, *3*, 3023−3030.
(21) Speirs, M.; Groeneveld, B.; Protesescu, L.; Piliego, C.; Kovalenko, M.; Loi, M. Hybrid Inorganic−Organic Tandem Solar Cells for Broad Absorption of The Solar Spectrum. *Phys. Chem. Chem. Phys.* **2014**, *16*, 7672−7676.
(22) Kim, T.; Gao, Y.; Hu, H.; Yan, B.; Ning, Z.; Jagadamma, L. K.; Zhao, K.; Kirmani, A. R.; Eid, J.; Adachi, M. M.; et al. Hybrid Tandem Solar Cells With Depleted-Heterojunction Quantum Dot and Polymer Bulk Heterojunction Subcells. *Nano Energy* **2015**, *17*, 196−205.
(23) Aqoma, H.; Azmi, R.; Oh, S.-H.; Jang, S.-Y. Solution-Processed Colloidal Quantum Dot/Organic Hybrid Tandem Photovoltaic Devices with 8.3% Efficiency. *Nano Energy* **2017**, *31*, 403−409.
(24) Tong, J.; Yang, X.; Xu, Y.; Li, W.; Tang, J.; Song, H.; Zhou, Y. Efficient Top-Illuminated Organic-Quantum Dots Hybrid Tandem Solar Cells with Complementary Absorption. *ACS Photonics* **2017**, *4*, 1172−1177.
(25) Kim, T.; Palmiano, E.; Liang, R.-Z.; Hu, H.; Murali, B.; Kirmani, A. R.; Firdaus, Y.; Gao, Y.; Sheikh, A.; Yuan, M.; et al. Hybrid Tandem Quantum Dot/Organic Photovoltaic Cells with Complementary Near Infrared Absorption. *Appl. Phys. Lett.* **2017**, *110*, 223903.
(26) Li, Y.-L.; Yeh, P.-N.; Sharma, S.; Chen, S.-A. Promotion of Performances of Quantum Dot Solar Cell and its Tandem Solar Cell with Low Bandgap Polymer (PTB7-Th): PC_{71} BM by Water Vapor Treatment on Quantum Dot Layer on its Surface. *J. Mater. Chem. A* **2017**, *5*, 21528−21535.
(27) Pattantyus-Abraham, A. G.; Kramer, I. J.; Barkhouse, A. R.; Wang, X.; Konstantatos, G.; Debnath, R.; Levina, L.; Raabe, I.; Nazeeruddin, M. K.; Grätzel, M.; et al. Depleted-Heterojunction Colloidal Quantum Dot Solar Cells. *ACS Nano* **2010**, *4*, 3374−3380.
(28) Barkhouse, D. A. R.; Kramer, I. J.; Wang, X.; Sargent, E. H. Dead Zones in Colloidal Quantum Dot Photovoltaics: Evidence and Implications. *Opt. Express* **2010**, *18*, A451−A457.
(29) He, Z.; Zhong, C.; Su, S.; Xu, M.; Wu, H.; Cao, Y. Enhanced Power-Conversion Efficiency in Polymer Solar Cells using an Inverted Device Structure. *Nat. Photonics* **2012**, *6*, 591−595.
(30) Lu, L.; Yu, L. Understanding Low Bandgap Polymer PTB7 and Optimizing Polymer Solar Cells Based on It. *Adv. Mater.* **2014**, *26*, 4413−4430.
(31) Foster, S.; Deledalle, F.; Mitani, A.; Kimura, T.; Kim, K. B.; Okachi, T.; Kirchartz, T.; Oguma, J.; Miyake, K.; Durrant, J. R.; et al. Electron Collection as a Limit to Polymer:PCBM Solar Cell Efficiency: Effect of Blend Microstructure on Carrier Mobility and Device Performance in PTB7:PCBM. *Adv. Energy Mater.* **2014**, *4*, 1400311.
(32) Ip, A. H.; Thon, S. M.; Hoogland, S.; Voznyy, O.; Zhitomirsky, D.; Debnath, R.; Levina, L.; Rollny, L. R.; Carey, G. H.; Fischer, A.; et al. Hybrid Passivated Colloidal Quantum Dot Solids. *Nat. Nanotechnol.* **2012**, *7*, 577−582.
(33) Kirmani, A. R.; Carey, G. H.; Abdelsamie, M.; Yan, B.; Cha, D.; Rollny, L. R.; Cui, X.; Sargent, E. H.; Amassian, A. Effect of Solvent Environment on Colloidal-Quantum-Dot Solar-Cell Manufacturability and Performance. *Adv. Mater.* **2014**, *26*, 4717−4723.
(34) Zhao, K.; Wodo, O.; Ren, D.; Khan, H. U.; Niazi, M. R.; Hu, H.; Abdelsamie, M.; Li, R.; Li, E. Q.; Yu, L.; et al. Vertical Phase Separation in Small Molecule:Polymer Blend Organic Thin Film Transistors Can Be Dynamically Controlled. *Adv. Funct. Mater.* **2016**, *26*, 1737−1746.
(35) Derue, L.; Dautel, O.; Tournebize, A.; Drees, M.; Pan, H.; Berthumeyrie, S.; Pavageau, B.; Cloutet, E.; Chambon, S.; Hirsch, L.; et al. Thermal Stabilisation of Polymer−Fullerene Bulk Heterojunction Morphology for Efficient Photovoltaic Solar Cells. *Adv. Mater.* **2014**, *26*, 5831−5838.
(36) Diroll, B. T.; Ma, X.; Wu, Y.; Murray, C. B. Anisotropic Cracking of Nanocrystal Superlattices. *Nano Lett.* **2017**, *17*, 6501−6506.
(37) Jagadamma, L. K.; Abdelsamie, M.; El Labban, A.; Aresu, E.; Ngongang Ndjawa, G. O.; Anjum, D. H.; Cha, D.; Beaujuge, P. M.; Amassian, A. Efficient Inverted Bulk-Heterojunction Solar Cells from Low-Temperature Processing of Amorphous ZnO Buffer Layers. *J. Mater. Chem. A* **2014**, *2*, 13321−13331.
(38) Jagadamma, L. K.; Al-Senani, M.; El-Labban, A.; Gereige, I.; Ngongang Ndjawa, G. O.; Faria, J. C.; Kim, T.; Zhao, K.; Cruciani, F.; et al. Polymer Solar Cells with Efficiency > 10% Enabled via a Facile Solution-Processed Al-Doped ZnO Electron Transporting Layer. *Adv. Energy Mater.* **2015**, *5*, 1500204.
(39) Mali, S. S.; Hong, C. K.; Inamdar, A.; Im, H.; Shim, S. E. Efficient Planar n-i-p Type Heterojunction Flexible Perovskite Solar Cells with Sputtered TiO_2 Electron Transporting Layers. *Nanoscale* **2017**, *9*, 3095−3104.
(40) Kim, T.-S.; Na, S.-I.; Oh, S.-H.; Kang, R.; Yu, B.-K.; Yeo, J.-S.; Lee, J.; Kim, D.-Y. All-Solution-Processed ITO-Free Polymer Solar Cells Fabricated on Copper Sheets. *Sol. Energy Mater. Sol. Cells* **2012**, *98*, 168−171.
(41) Schmidt, H.; Flügge, H.; Winkler, T.; Bülow, T.; Riedl, T.; Kowalsky, W. Efficient Semitransparent Inverted Organic Solar Cells with Indium Tin Oxide Top Electrode. *Appl. Phys. Lett.* **2009**, *94*, 243302.
(42) Gupta, D.; Wienk, M. M.; Janssen, R. A. Indium Tin Zxide-Free Tandem Polymer Solar Cells on Opaque Substrates with Top Illumination. *ACS Appl. Mater. Interfaces* **2014**, *6*, 13937−13944.
(43) Zheng, Z.; Zhang, S.; Zhang, M.; Zhao, K.; Ye, L.; Chen, Y.; Yang, B.; Hou, J. Highly Efficient Tandem Polymer Solar Cells with a Photovoltaic Response in the Visible Light Range. *Adv. Mater.* **2015**, *27*, 1189−1194.
(44) Martínez-Otero, A.; Liu, Q.; Mantilla-Perez, P.; Bajo, M. M.; Martorell, J. An Extremely Thin and Robust Interconnecting Layer Providing 76% Fill Factor in a Tandem Polymer Solar Cell Architecture. *J. Mater. Chem. A* **2015**, *3*, 10681−10686.
(45) Guyot-Sionnest, P. Electrical Transport in Colloidal Quantum Dot Films. *J. Phys. Chem. Lett.* **2012**, *3*, 1169−1175.

DOI: 10.1021/acsenergylett.8b00460
ACS Energy Lett. 2018, 3, 1307−1314